J Therm Spray Tech (2025) 34:1452–1462
https://doi.org/10.1007/s11666-025-01937-1

ORIGINAL RESEARCH ARTICLE

Towards Highly Dense Yb-Silicate Microstructures Deposited by Air Plasma Spray for Environmental Barrier Coating Applications II: Plasma Gas Composition, Feedstock, and Anode Orifice Comparisons

Edward J. Gildersleeve V[1] · Emine Bakan[1] · Robert Vaßen[1]

Submitted: 2 October 2024 / in revised form: 10 January 2025 / Accepted: 10 January 2025 / Published online: 10 February 2025

Abstract In all air plasma sprayed (APS) environmental barrier coating (EBC) applications, the predominant goal is to achieve maximum coating density, gas tightness, and/or hermeticity prior to subjecting it to harsh environments (i.e., high-temperature impingement of high-velocity water vapor). The microstructures of APS coatings are historically understood to be influenced by the input processing parameters. Beyond the local deposition rate (surface speed, feeding rate) explored in Part I, there are further extrinsic processing parameters such as plasma gas composition, feedstock choice, and anode orifice dimensions which can be tuned, but have not been fully explored in the context of EBCs. Screening these ancillary extrinsic inputs in a rigorous and systematic way presents challenges in determining which control variable(s) to select to gain meaningful insights. A constant particle temperature distribution (not average particle temperature) in the spray stream was held as a constraint, and the aforementioned extrinsic parameters were varied. As in Part I, a qualitative microstructural approach toward examining the presence (or absence) of advantageous vertical thin microcracks in the as-deposited coating was taken. For certain conditions, a Dense Vertically Macrocracked structure was achieved. Concurrent synthesis of these results offers further insights into process selection and parameter design can be gained.

Keywords APS · EBCs · feedstock comparison · hermeticity · microstructural evolution · plasma gas composition · $Yb_2Si_2O_7$

✉ Emine Bakan
e.bakan@fz-juelich.de

[1] Forschungszentrum Jülich GmbH, Institute of Energy Materials and Devices (IMD-2), 52425 Jülich, Germany

Introduction

In all air plasma sprayed (APS) environmental barrier coating (EBC) applications for gas turbines, the predominant desire is to obtain a coating with maximum gas tightness and hermeticity. This is a consequence of the need to protect SiC based ceramic matrix composite (CMC) components from the high-temperature impingement of water vapor which is formed as a combustion byproduct (Ref 1, 2). The challenge in achieving maximum density stems from the nature of the plasma spray processing of ceramic coatings—which creates inherently defective, porous structures due to the rapid solidification and successive buildup of impacting molten droplets of material (Ref 3-6). In the case of APS EBCs, it is therefore necessary to tune the process toward fabricating the densest possible microstructure by suppressing these aforementioned defects and pore-forming mechanisms that take place during spraying. However, it is not a straightforward task to find spraying conditions that yield dense—but not deleteriously cracked—coatings. This is in part because the spraying conditions that are most likely to yield highly dense structures can also easily form coatings that develop through-thickness macro segmentation cracks (i.e., Dense Vertically Cracked, DVC coatings) (Ref 7-11).

From a practical perspective, the ideal APS EBC spraying condition is one that approaches the threshold of making a DVC structure, but suppresses the onset and propagation of segmentation cracks. Yet there are intrinsic properties of EBC materials that make this a nontrivial effort. For instance, modern EBC materials are rare earth disilicates ($RE_2Si_2O_7$) which all deposit—notwithstanding unconventional spraying methodologies such as spraying into a furnace—as amorphous glass-ceramics (Ref 12-16). This implies a level of intrinsic brittleness to the as-

deposited EBC that is not present in, for example, polycrystalline ceramics such as yttria-stabilized zirconia. Therefore, when considering the buildup of available elastic strain energy during spray processing to form cracks, processing conditions must be tailored to take into account the intrinsically low energy release rate for fracture of the amorphous disilicate materials (Ref 17). As a result, EBC process selection in the plasma spraying space is inherently challenging.

In Part I of this work, one major conclusion was that the as-deposited APS EBC microstructure must not possess specific features that cannot be annihilated during the inevitable post-fabrication crystallization heat treatment. Due to the insufficient driving forces for densification, horizontal cracks and/or delaminations in the as-deposited coating microstructure are completely undesirable (Ref 18). It was found in Part I that there is a correlation between the inflight decomposition of the EBC material (in this case $Yb_2Si_2O_7$), the formation of monosilicate layer(s), and the crack pattern in a cross-sectional microstructure (Ref 19). Lower feeding rates and removing the fine fraction of the $Yb_2Si_2O_7$ were found to be two simultaneous measures that could be taken to mitigate these undesirable features. However, there are further processing parameters in the plasma spraying space to explore and manipulate; for instance, in scenarios wherein reduced feeding rates or feedstock sieving are not an option. In exploring these other processing parameters, a deeper understanding of how the as-deposited APS EBC microstructure can be controlled to achieve the most desirable outcome post-crystallization should be obtained.

Among the alternative parameters of interest, plasma gas composition (i.e., Ar-H_2 plasmas versus Ar-He plasmas), nozzle orifice dimension, and choice of feedstock lot/supplier all are surmisable to have an influence in the as-deposited EBC microstructure. However, there are foreseeable caveats to comparing these parameters against one another—the most obvious being how to choose a control variable(s) that would allow meaningful comparisons between different microstructures and the input process parameters. In Part I, maintaining a consistent particle temperature distribution (not average particle temperature) within the spray stream allowed for such comparisons. In this way, the supposed kinetics of disilicate-to-monosilicate inflight volatilization could be somewhat controlled. Moreover, deposition rates (and subsequently buildup stresses and the storage of available elastic strain energy) are rigorously controlled with this approach. Therefore, the same rationale was carried over into this study: wherein for different plasma gas compositions, feedstocks, and nozzle orifice dimensions, the plasma gun parameters were manipulated to achieve the same particle temperature distributions. From the results, a deeper understanding and database of parametric influences beyond the local deposition rate on as-deposited APS EBC microstructure and how this translates to the final crystallized microstructure can be ascertained.

Materials and Method

Yb-silicate coatings were manufactured by using two commercial Yb2Si2O7 feedstocks—hereafter designated A and B ($d_{10}/d_{50}/d_{90}$ = 18/40/66 µm, Oerlikon Metco, Westbury, NY; and $d_{10}/d_{50}/d_{90}$ = 14/28/57 µm, Höganäs, Sweden) in a MultiCoat system (Oerlikon Metco, Wohlen, Switzerland) with a three-cathode TriplexPro 210 cascaded plasma spray torch, mounted on a six-axis robot (IRB 2400, ABB, Switzerland). One $Yb_2Si_2O_7$ feedstock did not contain any secondary Yb_2SiO_5 phases (feedstock B), while the other (feedstock A) did; the XRD diffractogram of the powder can be found in the supplementary files of Part I (Ref 19). The plasma spray conditions are shown in Tables 1, 2. Once again it was necessary to constrain the final as-deposited coating thickness as rigorously as possible, so as to avoid undesired microstructural artifacts due to wildly different coating thicknesses (Ref 17). The experiments were systematically chosen in an effort to isolate the individual effects of plasma gas composition and nozzle orifice dimension, while simultaneously resolving their individual contribution to the as-deposited microstructure. For the robot toolpath, a typical ladder-style meander pattern was used to deposit the coatings in this study. In the case of the TriplexPro 210 torch, the three most common nozzle orifice dimensions—6.5 mm, 9 mm, and 11 mm—can only be utilized and compared simultaneously if an Ar-He plasma is chosen per the manufacturer's recommendations. The meander width was 200 mm for all experiments with a step size of 2 mm. In total 16 strokes were used to cover the entire surface of 25x25x3 mm Si bond-coated sintered α-SiC substrates (Saint Gobain Ceramics, Niagara Falls, NY). Si bond coat spraying conditions and feedstock information can be found elsewhere (Ref 20).

Specimen temperatures were measured during some of the depositions from the front and back side of the specimen using a NiCr thermocouple (Omega Engineering, Deckenpfronn, Germany, data acquisition 1 Hz) attached to the back of the samples as well as an infrared camera (Xi 400, Optris, Berlin, Germany, data acquisition 30 Hz) from

Table 1 $Yb_2Si_2O_7$ feedstock air plasma spray conditions

Spray parameters	Plasma condition 1	Plasma condition 2	Plasma condition 3	Plasma condition 4
Plasma gas composition	49 slpm Ar/1slpm H_2	46 slpm Ar / 4 slpm He	46 slpm Ar / 4 slpm He	46 slpm Ar / 4 slpm He
Spray current	300 A	450 A	435 A	325 A
Spray distance	90 mm	90 mm	90 mm	90 mm
Nozzle diameter	9 mm	9 mm	6.5 mm	11 mm
Surface speed	250, 500 mm/s *varied*	250, 500 mm/s *varied*	250 mm/s	250 mm/s
Feeding rate	2.7-23.1 g/min *varied*	2.7-23.1 g/min *varied*	2.7 g/min	2.7 g/min

Table 2 Coating experiment runs

Experiment	Plasma condition from Table 1	Surface speed (mm/s)	Feeding rate (g/min)	Feedstock chosen	Number of passes	Thickness per pass (μm/pass)	Average Particle Temperature (deg. C)	Average particle velocity (m/s)
#1	1	250	5.3	A	15	23	2176 + / − 198	187 + / − 24
#2	1	500	23.1	A	9	48	2169 + / − 200	171 + / − 20
#3	2	250	5.3	A	18	23	2167 + / − 135	183 + / − 24
#4	2	500	23.1	A	9	48	2186 + / − 149	180 + / − 21
#5	2	250	5.3	B	16	24	2158 + / − 139	188 + / − 24
#6	3	250	5.3	B	9	29	2172 + / − 292	279 + / − 34
#7	4	250	5.3	B	9	30	2152 + / − 203	167 + / − 28

Note that the number of passes was adjusted in each experiment to achieve a similar coating thickness (300-400 μm). The arithmetic average particle temperatures and velocities from the diagnostic measurements are also reported here

the specimen surface, assuming the emissivity as 1. Particle diagnostics during spraying were performed using the commercially available DPV Millenium Edition (Tecnar Inc., QC, Canada) (Ref 21). All experiments in this study adopted particle injection optimization methodologies to ensure uniform, consistent, and reproducible particle-plume interactions from run-to-run (Ref 22). During experiments with different nozzle orifice dimensions, the temperature distribution of the $Yb_2Si_2O_7$ powder from Part I of this work was used as a baseline, and the spray current was modulated to reach similar temperature distributions for Plasma Conditions 1-4. Note from Table 1, Condition 1, it was necessary to slightly alter the spray current from what was used in Part I in order to match particle temperature distributions for this study (i.e., from 325A in Part I with Powder B to 300 A here for Powder A) (Ref 19). Measurements of the particle state were taken at the center of the maximum counted particles within the plume. After deposition, a portion of the sprayed specimen was then placed in a box furnace in the air (Carbolite Gero, United Kingdom) to undergo heat treatments for crystallization. Metallographic cross-sections of the coatings were prepared for microstructural investigations via scanning electron microscopy (SEM, TM-3000, Hitachi, Tokyo, Japan).

Results and Discussion

Figure 1 shows the particle temperature distributions for all experiments considered in this study. As a reference point, the baseline particle temperature distributions for the starting parameter from Part I of this study is shown in the Figure. For all changes in plasma spray parameters (e.g., iterating between Ar-He and Ar-H_2 plasmas, spray current changes, nozzle changes, etc.), particle injection optimization was found to be both necessary and critical to ensure thermal treatment to the feedstock(s) were as similar as possible (Ref 22). In the case of the two different feedstocks, the requisite carrier gas flow rates for optimal injection when the plasma parameters were unchanged (i.e., Experiment #3 and Experiment #5 from Table 2) were found to be the same. This is somewhat surprising considering the two powders are similar in morphology but have slightly different size distributions. Nevertheless, clearly from Fig. 1, the injection optimization efforts contributed toward a highly self-consistent set of plasma spray streams with nearly equivalent temperature distributions of particles at the flow-center points of the spray plume(s). From these results in Fig. 1, two important conclusions can be drawn: first, the thermal contribution of

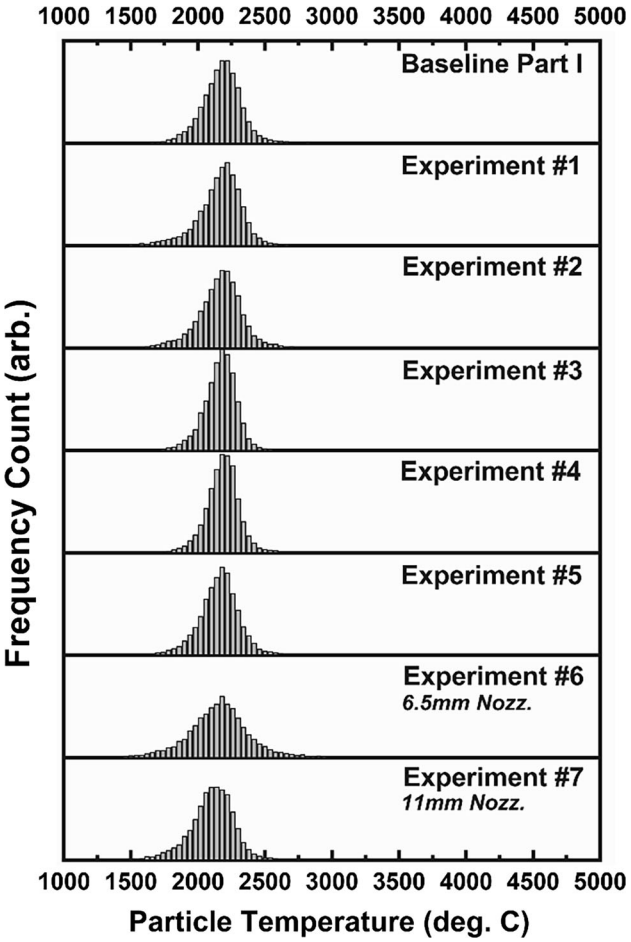

Fig. 1 Particle temperature distributions for all the experiments shown in Table 1. A reference dataset to the temperature distributions from Part I of this study is included as a baseline (Ref 19)

the individual particles (for spray experiments with equivalent feeding rates) to the receiving substrate should be equivalent. Second, none of these seven experiments, other than perhaps Experiments #6 and #7 which use different nozzle orifice dimensions, should yield particles with substantially different thermal histories. These two interpretations become critical when examining the subsequent microstructural results of the APS EBCs.

Figure 2 shows the as-deposited microstructures of the first four spray experiments (i.e., the plasma gas composition comparison study) for the APS $Yb_2Si_2O_7$ EBCs. At first glance, the Ar-H_2 EBCs of Fig. 2(a), (a1) (b), and (b1) seem fairly similar to the results obtained in Part I of this paper. That is, there are a combination of vertical and horizontal microcracks present in the microstructure. In addition, there seem to be qualitatively more horizontal defects (that were deemed deleterious in the prior study) in both of the sprayed coatings. These horizontal defects are shown by arrows in Fig. 2(a), (a1), (b) and (b1). Examining Fig. 1, it could be argued that there are slight differences in the lower end of the temperature distributions of Experiments #1 and #2 as compared to the baseline distribution from Part I's work using Powder B. Examining the particle size distributions of the two powders shows Powder A to be marginally coarser, which would explain why there is a slight increase in the amount of colder particles in the spray stream. This slight increase in colder particle concentration in the spray plume may also contribute to the marginally poorer intersplat bonding in the coatings from Fig. 2 as compared to the prior study due to an overall reduced degree of droplet melting (Ref 23, 24). It is unclear at this time whether this is a consequence of the alternative feedstock distributor or merely within the noise of cross-sectional microscopy.

More significant from Fig. 2 is the marked difference between the Ar-H_2 and Ar-He microstructures for the two APS EBCs. It should be noted that the only difference between the two experiments within a plasma gas composition dataset from this Figure (i.e., Experiment #1 vs. #2 or Experiment #3 vs. #4) is the local deposition rate—which was modulated in the same way as the previous part of this work. Irrespective of the local deposition rate, the Ar-He coatings clearly have two substantial differences in the as-deposited microstructure. First, the Ar-He coatings have substantially less through-thickness vertical intralamellar microcracks. Moreover, in place of these microcracks, larger through-thickness segmentation cracks have formed in the EBCs. Second, the interlamellar bonding quality between the individual splats appears to be substantially greater than in the case of the Ar-H_2 sprayed EBCs. These two differences are especially unexpected when noting from Table 2 that the deposition rates (in μm/pass) of the four EBCs in Fig. 2 are all comparable irrespective of plasma gas composition.

As previously mentioned, the temperature distributions of the particles in these experiments are nearly identical (Fig. 1); therefore, not only are the comparable deposition rates from Table 2 sensible, but the thermal contribution of the impinging droplets to the specimen surface upon impact and solidification can be assumed to be nearly the same. In Part I of this study, the deposition temperature on the surface and backside of the substrates was examined to identify whether microstructural differences were a consequence of enhanced bonding due to higher deposition temperatures as seen in past works (Ref 3, 16, 18, 25-29). However, in the prior case of Part I, no substantial difference in deposition temperatures was identified that could justify the differences observed in the microstructure.

Figure 3 shows the representative deposition temperature data for conditions equivalent to the Ar-H2 Experiment #1 and the Ar-He Experiment #3 from Table 2 and Fig. 2(a), (c), respectively. Clearly from Fig. 3, the deposition temperatures for the Ar-He spraying parameter are

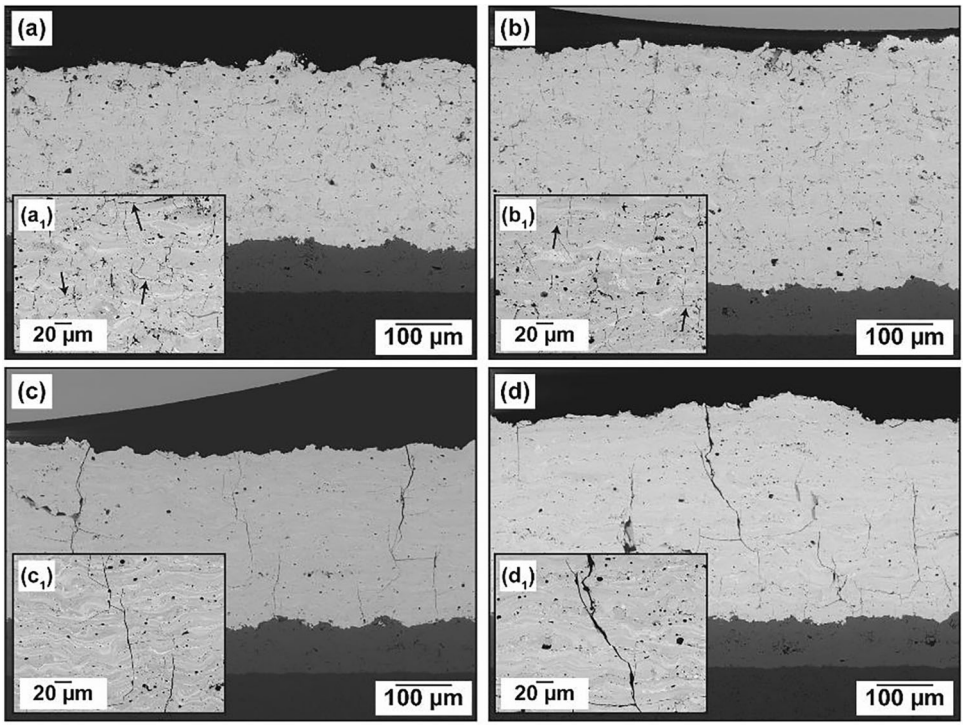

Fig. 2 As-deposited backscatter SEM microstructures of (a, a1) Experiment #1, (b, b1) Experiment #2, (c, c1) Experiment #3, and (d, d1) Experiment #4 from Table 2. Arrows indicate locations, where intrasplat bonding is poor and horizontal cracks/ delaminations appear

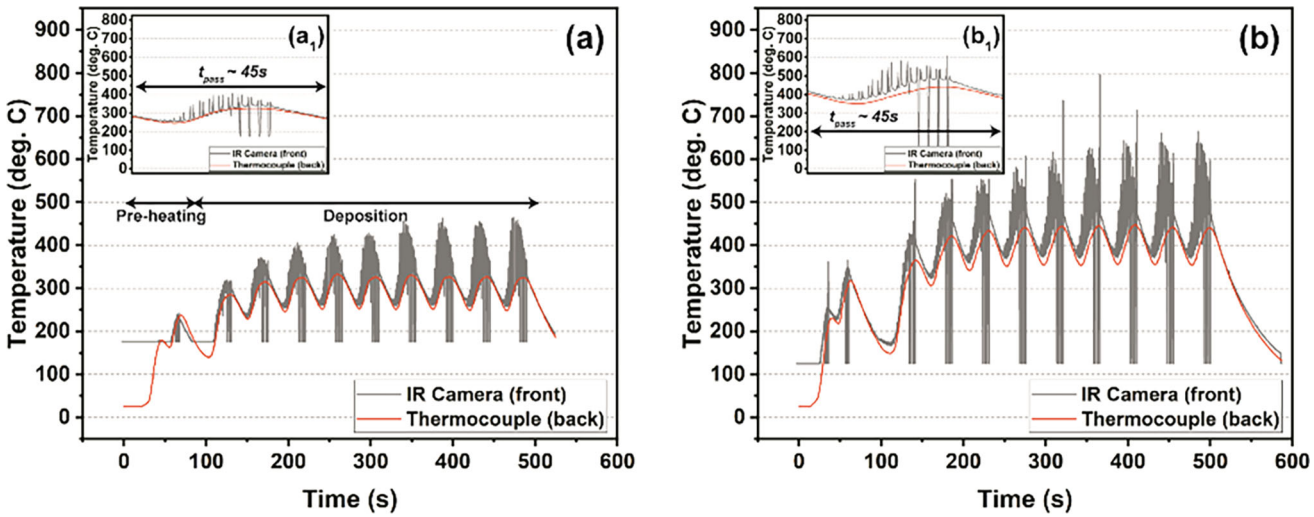

Fig. 3 Representative deposition temperature data for (a, a1) an equivalent spray condition to Experiment #1 (Ar-H2 plasma) and (b, b1) an equivalent spray condition to Experiment #3 (Ar-He plasma). The inset plots depict the temperatures observed for a single deposition pass

higher both overall as well as at the temperature peaks that were observed on the frontside. Moreover, unlike in the Ar-H_2 Experiment #1 (Fig. 3a, a1), there is a clear, albeit somewhat small, through-thickness thermal gradient throughout the deposition of the Ar-He Experiment #3 (Fig. 3b, b1). Given the near-equivalence in the particle temperature distributions and the equivalent measured deposition rate (Table 2) for these two spraying conditions, the difference in deposition temperatures is quite surprising. However, the observed microstructure results from Fig. 2 corroboratively suggest significant differences in deposition temperature. For example, the deposition temperatures (where maximum temperature peaks on the surface reach ~ 450 °C for the Ar-H_2 Experiment #1 and ~ 650 °C for the Ar-He Experiment #3) seem to be different enough that enhanced intersplat bonding of the $Yb_2Si_2O_7$ droplets could be achieved in the hotter Ar-He Experiment. It is surmisable to consider with higher frequency data acquisitions on the surface (above 30 Hz), resolving more substantial local deposition temperature

differences could be possible. What is more, the intersplat bonding was enhanced to such a degree that through-thickness segmentation could occur during the deposition of the material, as has been seen in prior studies (Ref 7, 8, 10). It is important to reiterate the aforementioned intrinsic brittleness of an amorphous glass-ceramic in the context of these microstructural results. Clearly, there is an extreme sensitivity to processing conditions that drives microstructure formation from dense and microcracked to dense with macrosegmentation cracks, which can draw back to subtle differences in deposition temperature. Essentially, at higher deposition temperatures, where the energy release rates for fracture have been measured to be higher in other studies, an intrinsically brittle amorphous material will be more likely to sustain segmentation cracking (Ref 7, 8, 17).

Given the particle thermal contribution to the specimen is assumed to be similar for the two spraying conditions, an alternative source of thermal load to the specimen must be the cause of the enhanced deposition temperatures. It could be said that utilizing the higher spraying current for the Ar-He conditions to match particle temperatures may have contributed to the overall enhanced deposition temperature. However, an increased arc current still does not directly explain the source of the clear thermal gradient through the specimen thickness during the deposition. It should be noted that, while not shown here, deposition temperature measurements were carried out for the two alternative nozzle experiments #6 and #7 from Table 2, and a through-thickness thermal gradient during deposition was observed in these cases as well. Therefore, considering the thermal gradient was never observed for Ar-H_2 plasma spraying conditions (neither in Part I nor in the data presented here), the anomaly must be a direct consequence of utilizing Ar-He plasma compositions. It is well-known that the thermal conductivity of an Ar-He plasma at the ionization temperatures of Ar and He is much higher than an Ar-H_2 plasma (Ref 30). Therefore, it could be said that the convective heat transfer of the plasma gases to the surface of the specimen is enhanced by the use of helium. This is further supported by the fact that the total plasma gas flow rate between the Ar-H_2 and Ar-He spraying conditions was kept constant for these experiments (i.e., 50slpm in total), which would imply that nearly the same moles of gas molecules are striking the specimen in both deposition conditions.

If the thermal gradient in Ar-He plasma spraying parameters is assumed to be present, then there are further driving forces that would inspire and enhance the growth of through-thickness segmentation cracks in the EBC during spraying, similar to what has been identified in past literature focusing on deliberately fabricating segmented coatings (Ref 7, 10, 11, 17). To that end, it becomes evident that Ar-He spraying conditions, at least for the cascaded plasma spray process as it was utilized here, must be tailored by keeping the enhanced propensity for segmentation cracking of amorphous brittle glass-ceramics in mind. The EBCs shown in Fig. 2 were in any case heat-treated for crystallization and to observe the microstructural evolution in the same way as was studied in Part I of this work.

Figure 4 shows the four APS EBCs from Experiments #1-4 in Table 2 after a standard single-step heat treatment, as described in Part I of this work. From Fig. 4, several important conclusions can be drawn. First, despite the seemingly wide crack opening dimension of the through-thickness segmentation cracks in the as-deposited Ar-He EBCs (Fig. 2(c), (c_1), (d) and (d_1), these cracks have nearly healed by virtue of the viscous flow, metastable to stable phase transformation and solid-state sintering mechanisms described elsewhere (Ref 18, 31). At higher magnifications (Fig. 4(c_1), (d_1), it is clear that these cracks are still present in the EBC. Additionally, the horizontal separations that were deemed deleterious in Part I of this work are still present in the Ar-He microstructures of Fig. 4(c_1), (d_1)—which could in principle be connected to other cracks/porosity in the microstructure and lead to a breach in hermeticity.

By contrast, the Ar-H_2 EBCs appear to have retained a significantly lower amount of cracks in the microstructure after heat treatment. It is important to reiterate that in the as-deposited state (Fig. 2), the Ar-He EBCs appeared well-bonded as compared to the Ar-H_2 EBCs, despite the through-thickness segmentation cracks. However, it would seem that after heat treatment, the Ar-H_2 EBCs from this set of coatings appear to be more likely to be gas tight, in the sense they do not seem to have as significant of horizontal cracking/separations in the microstructure. The exact mechanism that drives the divergence in crystallization and densification behavior between Ar-H_2 and Ar-He sprayed EBCs is beyond the scope of this paper. However, it is interesting to observe that the Ar-He EBCs (Fig. 4(c_1), (d_1)) have retained significantly more of the brighter (in backscatter contrast) monosilicate phase as compared to the Ar-H_2 EBC. This is a notable result, considering it is generally agreed that H_2 plasmas can exacerbate the inflight decomposition of rare earth disilicates, yet the Ar-He plasma qualitatively appears more decomposed (Ref 12, 13, 15). Nevertheless, an enhanced monosilicate content upon deposition could drive sintering-assisting stresses due to CTE mismatch strains within the coating during heat treatment. Detailed investigations of the crystallization pathway, interrupted heat treatments, time resolved x-ray diffraction, and dilatometric studies would all be required to more deeply understand why the Ar-He EBCs appear by microstructure to have retained

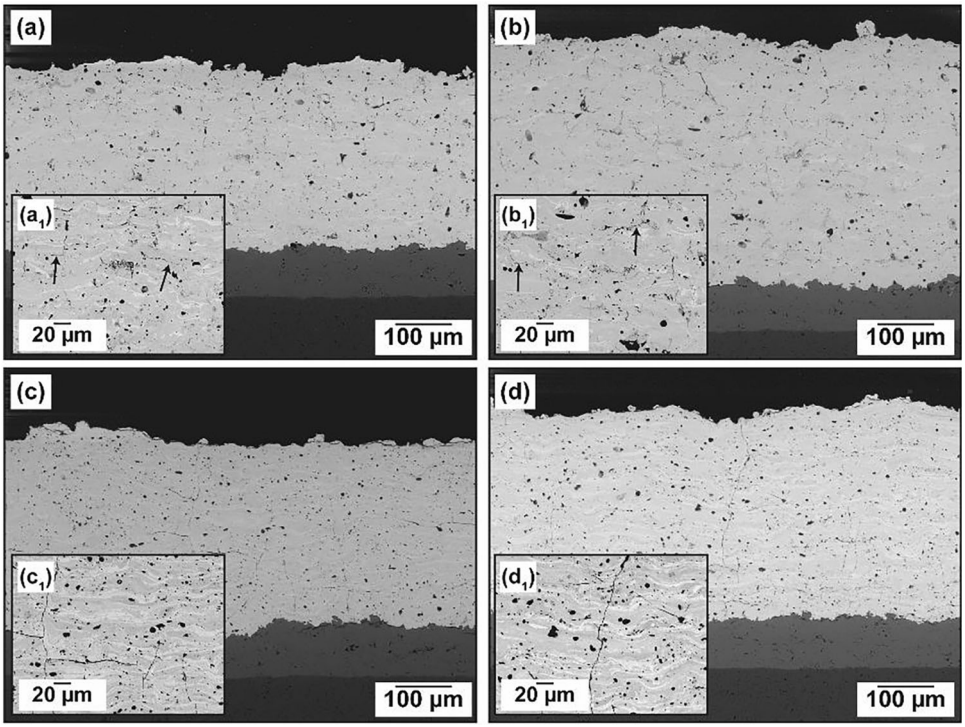

Fig. 4 Standard single-step heat-treated (1300 °C, 20 hr) microstructures of the APS EBCs shown in Fig. 2. Arrows indicate locations, where horizontal cracks/delaminations were not annihilated during the heat treatment

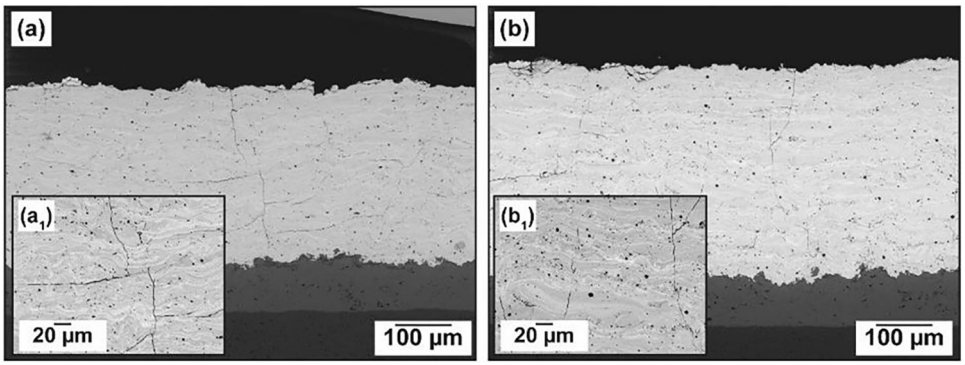

Fig. 5 2-step (975 °C, 40 hr; 1300 °C, 10 hr) heat-treated microstructures of the Ar-He sprayed EBCs. (a, a1) the EBC from Experiment #3, (b, b1) the EBC from Experiment #4 in Table 2

significantly more monosilicate phase, and whether or not that drives sintering-supportive stresses to form in the coatings.

For comprehensiveness, the Ar-He EBCs were also subjected to the 2-step heat treatment designed to control the viscous flow of the material. The microstructures after 2-step heat treatment are shown in Fig. 5 (Ref 18). As it was seen in Part I of this work, the horizontal cracks and separations that are present in the as-deposited microstructure are still seen here—due in part to reduce suppressed viscous flow during heat treatment (Ref 18). In addition, the vertical cracks in the EBCs after the 2-step heat treatment appear to be qualitatively more prominent at lower magnifications than after the standard heat treatment (Fig. 5(a), (b) vs. Fig. 4(c), (d))—which corroborates with the results seen in Part I of this work.

Beyond the Ar-H_2 and Ar-He comparison, coatings sprayed with different nozzle orifice diameters were also evaluated. For these comparisons, it was decided to use Powder B from Part I of this work. Fig. 6 shows the as-deposited coatings. It is important to note that per the manufacturer's recommendations, it is not possible to cross-compare spraying conditions with the TriplexPro cascaded plasma torch based on nozzle diameter unless an Ar-He plasma is used. Consequently, one cannot directly compare the baseline coating from Part I (9 mm, Ar-H2) without establishing an Ar-He analogous condition. Therefore, it was necessary to once again evaluate and assess whether the Ar-He conditions used in the prior experiments were self-consistent by matching particle temperature distributions. As was seen in Fig. 2, using an Ar-He plasma instead of an Ar-H_2 (Fig. 6(b), (b1) vs. Fig. 6

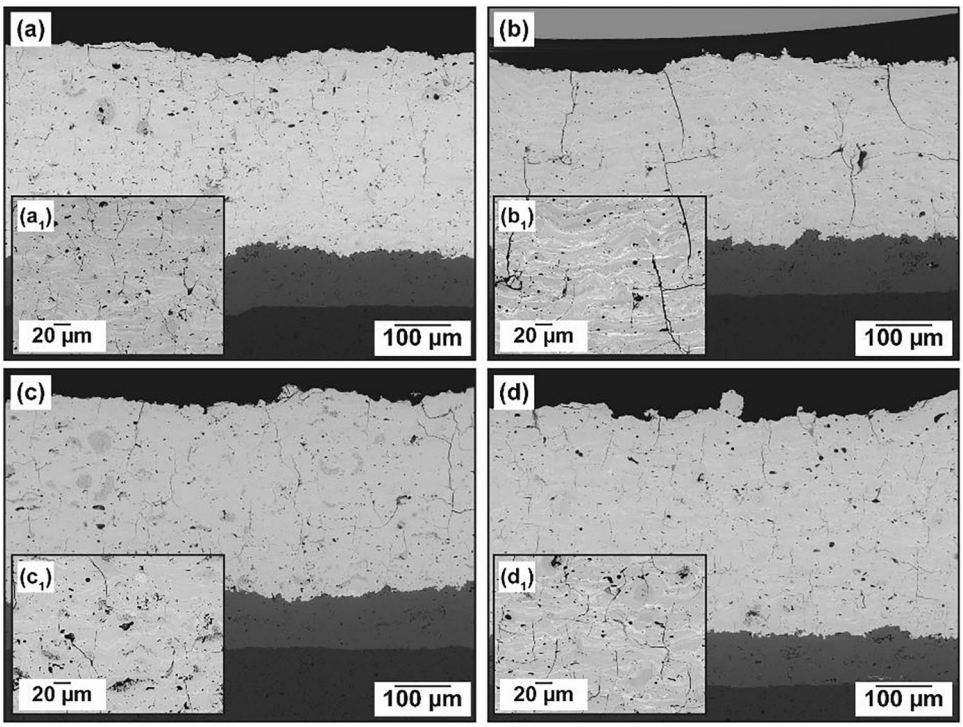

Fig. 6 As-deposited microstructures of (a, a1) the baseline Ar-H2 EBC from Part I of this work using a 9 mm anode, (b, b1) the temperature distribution matched Ar-He 9 mm anode EBC from Experiment #5 in Table 2, (c, c1) the temperature distribution matched Ar-He 6.5 mm anode EBC from Experiment #6 in Table 2, and (d, d1) the temperature distribution matched Ar-He 11 mm anode EBC from Experiment #7 in Table 2

(a), (a1), respectively) plasma yielded an EBC with through-thickness segmentation cracks as opposed to benign vertically-oriented microcracks. In fact, not only are the microstructures of Fig. 2(c), (c1), and Fig. 6(b), (b1) nearly indistinguishable, but their deposition rates, particle temperature distributions, and average particle temperatures and velocities were all comparable as well. Note that these results come in spite of utilizing different powders from different suppliers. This implies that the microstructural result is not dependent on powder or feedstock or where it originated; rather, it is more likely to be a fundamental difference associated with spraying EBCs with helium instead of hydrogen in cascaded plasmas.

Again from Fig. 1, it is clear that the particle states in Experiment #5 were well-aligned with the baseline condition from Part I of this work. Moreover, the use of different nozzle diameters for Experiments #6 and #7 nominally generated temperature distributions that were centered around a similar temperature as the other experiments. From Table 2, the particle velocities between the baseline and Experiment #5, 6, and 7 are evidently different. Using the 6.5 mm nozzle created a plasma stream containing particles of significantly higher velocities. Consequently, the temperature distribution from Fig. 1 of Experiment #6 has the lowest concentration of particles between 1800-2200 °C among all other conditions. This is likely a consequence of the individual particles having much different residence times in the flame due to their higher velocities. Comparatively, the 11 mm nozzle Experiment #7 in Fig. 1 has a temperature distribution more closely in alignment with the other experiments, while also showing lower particle velocities (Table 2).

These differences in temperature distribution and the implied differences in particle residence time due to different velocities are also evident from the microstructural comparison in Fig. 6. In the case of the higher particle velocities from Experiment #6, the microstructure of the as-sprayed EBC in Fig. 6(c), (c1) clearly shows two distinct features that are a consequence of reduced particle residence time. First, there is a higher degree of embedded unmolten/semi molten agglomerated particles in the coating (most clearly seen when comparing Fig. 6b with Fig. 6(c)). In addition, the through-thickness macrosegmentation cracks seen in Fig. 6b do not appear as readily in Fig. 6(c). This could be a combined effect of less efficient intrasplat bonding (seen when comparing Fig. 6(b1) with Fig. 6(c1)) inhibiting the coalescence and propagation of segmentation cracking during deposition of the coating (Ref 8, 17). Despite the similarities in the particle temperature distributions from Fig. 1, the higher particle velocities (Table 2) would undoubtedly reduce the overall molten content in the spray stream, explaining the presence of unmolten/semi molten particles within the coating (Ref 23). Aside from the particle molten content in the spray stream, while not shown here, the deposition temperatures of the 6.5 mm nozzle Experiment #6 were nominally lower

than the 9 mm nozzle Experiment #5—and this could also contribute to the reduced propensity for segmentation cracking in the coating (Ref 8, 9, 17).

In the case of the 11 mm nozzle Experiment #7, a lower spray current was needed to achieve the desired temperature distribution—likely because of the increased thermal output of the plasma torch as well as the lower overall velocity of the plasma gases and entrained particles. This also yielded a lower deposition temperature than the 9 mm nozzle Experiment #5 (Fig. 6(b), (b1)), and as such, no segmentation cracking can be seen in the coating. In fact, the cross-section of the 11 mm Ar-He coating in Fig. 6(d), (d1) appears qualitatively to be the closest among the three Ar-He candidates to the baseline Fig. 6(a), (a1). Moreover, the deposition temperature for the 11 mm nozzle Experiment #7 was the closest among all the Ar-He experiments to the Ar-H_2 baseline condition. Among all the Ar-He spraying conditions from Table 2, Experiment #7 appeared to have the lowest through-thickness thermal gradient during deposition. This could also contribute to the microstructural lack of through-thickness segmentation cracks seen in Fig. 6(d). These results concurrently suggest that even when deposition rate and particle temperature distributions are similar, the as-deposited microstructure of APS EBCs—and consequently the overall density of the crystallized microstructure—is heavily sensitive to extrinsic processing factors such as deposition temperatures.

Figure 7 shows the single-step heat-treated EBC microstructures from Fig. 6. Again as seen in the Part I and earlier results from this paper, the large horizontal cracks due to the macrosegmentation events of the Ar-He 9 mm-sprayed EBC were unable to close and heal during the heat treatment (Fig. 7(b), (b1)). Also, in agreement with Fig. 4, the macrosegmentation cracks that were present in the as-deposited state appear to have almost completely annihilated during the heat treatment.

In the case of the other nozzle diameter coatings, the 6.5 mm nozzle coating in Fig. 7(c), (c1) shows an unexpectedly high concentration of unhealed vertical microcracks after heat treatment (especially as compared to the baseline Fig. 7(a1)). This could be a result of at least two factors: first, due to the higher particle velocities and lower deposition temperatures, the aforementioned supposed-poor intersplat bonding and splat contact may have prevented the requisite viscous flow and solid-state sintering mechanisms for crack healing to properly occur (Ref 18, 26). For example, the higher unmolten particle content in the coating (XRD data of as-sprayed coatings with different nozzle diameters can be found in supplementary data) would conceivably increase the volumetric content of crystalline material within the coating, thereby suppressing viscous flow mechanisms during heat treatment (Ref 12, 13, 18).

The second possible contributor to the lack of microcrack healing in the 6.5 mm EBC can be seen when qualitatively comparing the backscatter contrast of the heat-treated EBCs in Fig. 7 at higher magnifications. Qualitatively, there seems to be less bright/monosilicate phase in the 6.5 mm EBC (Fig. 7(c1)) as compared to the other EBCs. This qualitative relationship also seems apparent

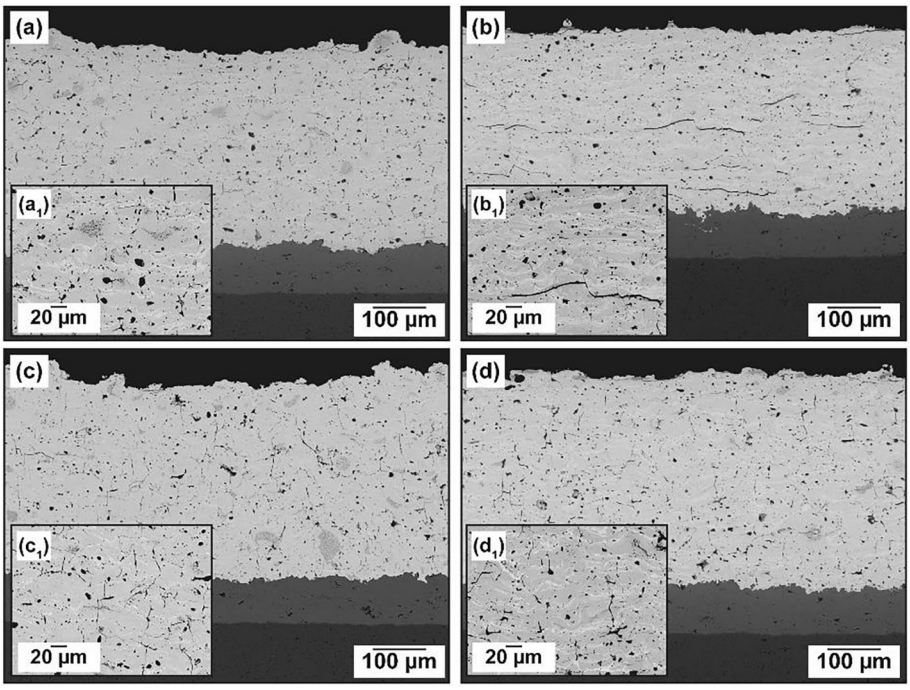

Fig. 7 Standard, single-step heat-treated (1300 °C, 20 hr) microstructures of (a, a1) the baseline Ar-H2 EBC from Part I of this work using a 9 mm anode, (b, b1) the temperature distribution matched Ar-He 9 mm anode EBC from Experiment #5 in Table 2, (c, c1) the temperature distribution matched Ar-He 6.5 mm anode EBC from Experiment #6 in Table 2, and (d, d1) the temperature distribution matched Ar-He 11 mm anode EBC from Experiment #7 in Table 2

when comparing Fig. 6(c1) to the other as-deposited EBCs. It is surmisable to consider the higher particle velocities (Table 2) and reduced residence time in the plasma flame contributed to a marginally reduced monosilicate content in the final EBC. With a smaller monosilicate content, the metastable to stable phase changes that contribute to large constrained volumetric changes (and therefore crack healing inducing stresses) should subsequently be reduced (Ref 18, 31). Nevertheless it should be mentioned that the overall lack of monosilicate content in the coating would also subsequently reduce the magnitude of the CTE-mismatch induced tensile residual stresses at room temperature—which would naturally drive any existing cracks in the microstructure to have smaller opening displacements (Ref 32). However, more detailed phase analysis and high-resolution microstructural studies would be required to definitively prove whether or not a plasma spray stream of faster, yet temperature distribution matched particles would yield a coating of statistically lower monosilicate content. While not shown here, it is important to note that all the 2-step heat treatments done on these EBCs showed similar results that were seen in Fig. 5 and Part I of this work.

These experimental results when examined conjunctively, along with what has been shown in Part I of this work, can serve as a framework from which establishing a roadmap for designing APS EBC plasma spraying conditions is plausible. Overarching conclusions such as the critical importance of eliminating horizontal (in 2-dimensions) cracking and delamination from the as-deposited EBC microstructure to ensure maximum density after crystallization heat treatment should drive future EBC spray parameter selection. Moreover, in this paper specifically, the sensitivity of APS EBCs (when nearly all else is held to be equal) to form macro-through-thickness-segmentation cracks during spraying with Ar-He cascaded plasmas should be considered to avoid the unwanted horizontal defects.

Conclusions

This work has examined the aspects of plasma spray processing, beyond local deposition rate, to augment what was presented in Part I of this effort. Specifically, the effects of plasma gas composition, anode orifice dimension, and complimentary studies to Part I on surface speed and feed rate using these new parameters were shown. The most notable findings from this work were as follows:

- Utilizing injection optimization principles, it was possible to develop unique spraying parameters—— that yielded similar particle temperature distributions (not just average particle temperatures)
- These temperature distribution matched conditions to the baseline condition from Part I in the paper yielded equivalent as-deposited microstructures, when the same Ar-H_2 parameter space was used—despite utilizing a different starting feedstock. The heat-treated microstructures of these coatings with dispersed vertical microcracks showed the highest apparent density in cross-section, which is consistent with the motivation of this work as well as the results shown in Part I.
- However, in the case of Ar-He spraying conditions, which needed higher arc currents to match the particle temperature distributions, higher deposition temperatures (and a through-thickness thermal gradient) were observed—as well as Dense Vertically Macrocracked as-deposited coatings. These macrocracks did not self-heal upon crystallization and annealing—which is again consistent with the motivation of this work as well as the results shown in Part I.
- Qualitatively, by backscatter contrast, the Ar-He EBCs appeared to retain a larger portion of the bright monosilicate phase after crystallization. Detailed phase analysis was beyond the scope of this study but can be considered as a future direction of research.

Different sized anodes (6.5 mm, 9 mm, and 11 mm) with particle temperature distribution matched spray conditions will yield substantially different as-deposited microstructural features. Smaller anodes increase particle velocity and reduce particle residence time, leading to the incorporation of more unmolten particles. Likewise, the backscatter contrast suggests less monosilicate phase retention in the smaller-anode coatings. Larger anodes with Ar-He appear to yield microstructures that are more in line with what was achieved with the standard anode and Ar-H2 conditions. In this case, both the particle temperature distributions and deposition temperatures were in line with one another—which serves as the governing aspects as to how these two different processing approaches yielded similar appearing coatings both before and after heat treatment.

Funding Open Access funding enabled and organized by Projekt DEAL.

Supplementary Information The online version contains supplementary material available at https://doi.org/10.1007/s11666-025-01937-1.

References

1. N.S. Jacobson, E.J. Opila, and K.N. Lee, Oxidation and Corrosion of Ceramics and Ceramic Matrix Composites, *Curr. Opin. Solid State Mater. Sci.*, 2001, **5**(4), p 301-309.
2. E.J. Opila et al., SiC Recession Caused by SiO_2 Scale Volatility under Combustion Conditions: II, Thermodynamics and Gaseous-Diffusion Model, *J. Am. Ceram. Soc.*, 1999, **82**(7), p 1826-1834.
3. S. Sampath and X. Jiang, Splat Formation and Microstructure Development During Plasma Spraying: Deposition Temperature Effects, *Mater. Sci. Eng. A*, 2001, **304-306**, p 144-150.
4. H. Herman, Plasma-Sprayed Coatings, *Sci. Am.*, 1988, **259**(3), p 112-117.
5. H. Herman, Plasma Spray Deposition Processes, *MRS Bull.*, 1988, **13**(12), p 60-67.
6. S. Sampath and H. Herman, Rapid Solidification and Microstructure Development During Plasma Spray Deposition, *J. Therm. Spray Technol.*, 1996, **5**(4), p 445-456.
7. S.V. Shinde et al., Segmentation Crack Formation Dynamics During Air Plasma Spraying of Zirconia, *Acta Mater.*, 2020, **183**, p 196-206.
8. S.V. Shinde and S. Sampath, Factors Governing Segmentation Crack Characteristics in Air Plasma Sprayed Ceramics, *J. Eur. Ceram. Soc.*, 2022, **42**(3), p 1077-1087.
9. R. Vassen, F. Traeger, and D. Stover, Correlation Between Spraying Conditions and Microcrack Density and Their Influence on Thermal Cycling Life of Thermal Barrier Coatings, *J. Therm. Spray Technol.*, 2004, **13**(3), p 396-404.
10. H.B. Guo, R. Vaßen, and D. Stöver, Atmospheric Plasma Sprayed Thick Thermal Barrier Coatings with High Segmentation Crack Density, *Surf. Coat. Technol.*, 2004, **186**(3), p 353-363.
11. M. Karger, R. Vaßen, and D. Stöver, Atmospheric Plasma Sprayed Thermal Barrier Coatings with High Segmentation Crack Densities: Spraying Process, Microstructure and Thermal Cycling Behavior, *Surf. Coat. Technol.*, 2011, **206**(1), p 16-23.
12. E. Bakan et al., $Yb_2Si_2O_7$ Environmental Barrier Coatings Deposited by Various Thermal Spray Techniques: A Preliminary Comparative Study, *J. Therm. Spray Technol.*, 2017, **26**(6), p 1011-1024.
13. E. Garcia, H. Lee, and S. Sampath, Phase and Microstructure Evolution in Plasma Sprayed $Yb_2Si_2O_7$ Coatings, *J. Eur. Ceram. Soc.*, 2019, **39**(4), p 1477-1486.
14. B.T. Richards and H.N.G. Wadley, Plasma Spray Deposition of Tri-Layer Environmental Barrier Coatings, *J. Eur. Ceram. Soc.*, 2014, **34**(12), p 3069-3083.
15. B.T. Richards, H. Zhao, and H.N.G. Wadley, Structure, Composition, and Defect Control during Plasma Spray Deposition of Ytterbium Silicate Coatings, *J. Mater. Sci.*, 2015, **50**(24), p 7939-7957.
16. R. Vaßen et al., Correlation of Process Conditions, Porosity Levels and Crystallinity in Atmospherically Plasma Sprayed $Yb_2Si_2O_7$ Environmental Barrier Coatings, *J. Compos. Sci.*, 2021, **5**(8), p 198.
17. S.V. Shinde and S. Sampath, Interplay Between Cracking and Delamination in Incrementally Deposited Plasma Sprayed Coatings, *Acta Mater.*, 2021, **215**, p 117074.
18. E. Bakan and R. Vaßen, Crack Healing Mechanisms in Atmospheric Plasma Sprayed Yb-silicate Coatings during Post-Process Heat Treatment, *J. Eur. Ceram. Soc.*, 2023, **43**(8), p 3684-3693.
19. E. Bakan, E.J. Gildersleeve V, and R. Vassen, Towards Highly Dense Yb-Silicate Microstructures Deposited by Air Plasma Spray for Environmental Barrier Coating Applications I: Influence of Local Deposition Rate. 2024: Under Review in the Journal of Thermal Spray Technology.
20. E. Bakan et al., Plasma Sprayed Duplex Ytterbium Disilicate/Monosilicate EBCs and the Transformation from Ytterbia to Ytterbium Monosilicate during Burner Rig Testing, *Corros. Sci.*, 2024, **235**, p 112174.
21. P. Gougeon and C. Moreau, In-Flight Particle Surface Temperature Measurement: Influence of the Plasma Light Scattered by the Particles, *J. Therm. Spray Technol.*, 1993, **2**(3), p 229-233.
22. V. Srinivasan et al., Particle Injection in Direct Current Air Plasma Spray: Salient Observations and Optimization Strategies, *Plasma Chem. Plasma Process.*, 2007, **27**(5), p 609-623.
23. H. Zhang et al., Melting Behavior of In-Flight Particles and Its Effects on Splat Morphology in Plasma Spraying, in *ASME 2002 International Mechanical Engineering Congress and Exposition*. 2002: New Orleans, Louisiana USA. p. 309-316.
24. W. Zhang and S. Sampath, A Universal Method for Representation of In-Flight Particle Characteristics in Thermal Spray Processes, *J. Therm. Spray Technol.*, 2009, **18**(1), p 23-34.
25. P. Fauchais et al., Knowledge Concerning Splat Formation: An Invited Review, *J. Therm. Spray Technol.*, 2004, **13**(3), p 337-360.
26. E. Bakan et al., Effect of Processing on High-Velocity Water Vapor Recession Behavior of Yb-Silicate Environmental Barrier Coatings, *J. Eur. Ceram. Soc.*, 2019, **39**(4), p 1507-1513.
27. H. Wang et al., Microstructure and Phase Composition Evolution of Dual-Phase Ytterbium Silicate Coatings Plasma Sprayed from Stoichiometric $Yb_2Si_2O_7$ Feedstock Powder, *Surface Coat. Technol.*, 2022, **437**, p 128373.
28. A. Lynam et al., Atmospheric Plasma Spraying of Ytterbium Disilicate for Abradable and Environmental Barrier Coatings: a Story of Processing-Microstructure Relationships, *Ceram. Int.*, 2023, **49**(13), p 22232-22243.
29. B. Li et al., Influence of Spraying Power on Microstructure, Phase Composition and Nanomechanical Properties of Plasma-Sprayed Nanostructured Yb-Silicate Environmental Barrier Coatings, *Surf. Coat. Technol.*, 2024, **478**, p 130450.
30. B. Pateyron et al., Thermodynamic and Transport Properties of Ar-H2 and Ar-He Plasma Gases used for Spraying at Atmospheric Pressure. I: Properties of the Mixtures, *Plasma Chem. Plasma Process.*, 1992, **12**(4), p 421-448.
31. E. Bakan, Y.J. Sohn, and R. Vaßen, Metastable to Stable Phase Transformation in Atmospheric Plasma Sprayed Yb-Silicate Coating During Post-Heat Treatment, *Scripta Mater.*, 2023, **225**, p 115169.
32. T.W. Clyne and S.C. Gill, Residual Stresses in Thermal Spray Coatings and Their Effect on Interfacial Adhesion: A Review of Recent Work, *J. Therm. Spray Technol.*, 1996, **5**(4), p 401.